

# Motion-compensated hand-held common-path Fourier-domain optical coherence tomography probe for image-guided intervention

Yong Huang,\* Xuan Liu, Cheol Song, and Jin U. Kang

Department of Electrical and Computer Engineering, The Johns Hopkins University, 3400 North Charles Street, Baltimore, MD 21218, USA

\*yhuang60@jhu.edu

**Abstract:** A motion-compensated, hand-held, common-path, Fourier-domain optical coherence tomography imaging probe has been developed for image-guided intervention during microsurgery. A hand-held prototype instrument was achieved by integrating an imaging fiber probe inside a stainless steel needle and attached to the ceramic shaft of a piezoelectric motor housed in an aluminum handle. The fiber probe obtains A-scan images. The distance information was extracted from the A-scans to track the sample surface distance and a fixed distance was maintained by a feedback motor control which effectively compensated hand tremor and target movements in the axial direction. Real-time data acquisition, processing, motion compensation, and image visualization and saving were implemented on a custom CPU-GPU hybrid architecture. We performed  $10\times$  zero padding to the raw spectrum to obtain  $0.16\text{ }\mu\text{m}$  position accuracy with a compensation rate of 460 Hz. The root-mean-square error of hand-held distance variation from target position was measured to be  $2.93\text{ }\mu\text{m}$ . We used a cross-correlation maximization-based shift correction algorithm for topology correction. To validate the system, we performed free-hand OCT M-scan imaging using various samples.

© 2012 Optical Society of America

**OCIS codes:** (100.2000) Digital image processing; (110.4500) Optical coherence tomography; (170.3890) Medical optics instrumentation.

## References and links

1. D. Huang, E. A. Swanson, C. P. Lin, J. S. Schuman, W. G. Stinson, W. Chang, M. R. Hee, T. Flotte, K. Gregory, C. A. Puliafito, and J. G. Fujimoto, "Optical coherence tomography," *Science* **254**(5035), 1178–1181 (1991).
2. B. E. Bouma, *Handbook of Optical Coherence Tomography* (New York: Marcel Dekker, 2001).
3. A. M. Zysk, F. T. Nguyen, A. L. Oldenburg, D. L. Marks, and S. A. Boppart, "Optical coherence tomography: a review of clinical development from bench to bedside," *J. Biomed. Opt.* **12**(5), 051403 (2007).
4. S. A. Boppart, W. Luo, D. L. Marks, and K. W. Singletary, "Optical coherence tomography: feasibility for basic research and image-guided surgery of breast cancer," *Breast Cancer Res. Treat.* **84**(2), 85–97 (2004).
5. M. S. Jafri, R. Tang, and C. M. Tang, "Optical coherence tomography guided neurosurgical procedures in small rodents," *J. Neurosci. Methods* **176**(2), 85–95 (2009).
6. A. Ahmad, S. G. Adie, E. J. Chaney, U. Sharma, and S. A. Boppart, "Cross-correlation-based image acquisition technique for manually-scanned optical coherence tomography," *Opt. Express* **17**(10), 8125–8136 (2009).
7. J. U. Kang, Y. Huang, K. Zhang, Z. Ibrahim, J. Cha, W. P. A. Lee, G. Brandacher, and P. L. Gehlbach, "Real-time three-dimensional Fourier-domain optical coherence tomography video image guided microsurgies," *J. Biomed. Opt.* **17**(8), 081403 (2012).
8. K. Zhang and J. U. Kang, "Real-time intraoperative 4D full-range FD-OCT based on the dual graphics processing units architecture for microsurgery guidance," *Biomed. Opt. Express* **2**(4), 764–770 (2011).
9. Z. P. Chen, T. E. Milner, S. Srinivas, X. Wang, A. Malekafzali, M. J. van Gemert, and J. S. Nelson, "Noninvasive imaging of in vivo blood flow velocity using optical Doppler tomography," *Opt. Lett.* **22**(14), 1119–1121 (1997).
10. B. C. Becker, R. A. MacLachlan, and C. N. Riviere, "State estimation and feedforward tremor suppression for a handheld micromanipulator with a Kalman filter," in *2011 IEEE/RSJ International Conference on Intelligent Robots and Systems (IROS)* (IEEE, 2011), pp. 5160–5165.

11. S. A. Boppart, B. E. Bouma, C. Pitris, G. J. Tearney, J. G. Fujimoto, and M. E. Brezinski, "Forward-imaging instruments for optical coherence tomography," *Opt. Lett.* **22**(21), 1618–1620 (1997).
12. W. G. Jung, J. Zhang, L. Wang, P. Wilder-Smith, Z. P. Chen, D. T. McCormick, and N. C. Tien, "Three-dimensional optical coherence tomography employing a 2-axis microelectromechanical scanning mirror," *IEEE J. Sel. Top. Quantum Electron.* **11**(4), 806–810 (2005).
13. S. Han, M. V. Sarunic, J. Wu, M. Humayun, and C. H. Yang, "Handheld forward-imaging needle endoscope for ophthalmic optical coherence tomography inspection," *J. Biomed. Opt.* **13**(2), 020505 (2008).
14. L. Huo, J. Xi, Y. Wu, and X. Li, "Forward-viewing resonant fiber-optic scanning endoscope of appropriate scanning speed for 3D OCT imaging," *Opt. Express* **18**(14), 14375–14384 (2010).
15. H. C. Park, C. Song, M. Kang, Y. Jeong, and K. H. Jeong, "Forward imaging OCT endoscopic catheter based on MEMS lens scanning," *Opt. Lett.* **37**(13), 2673–2675 (2012).
16. X. Liu, Y. Huang, and J. U. Kang, "Distortion-free freehand-scanning OCT implemented with real-time scanning speed variance correction," *Opt. Express* **20**(15), 16567–16583 (2012).
17. S. P. N. Singh and C. N. Riviere, "Physiological tremor during retinal microsurgery," in *Proceedings of the IEEE 28th Annual Northeast Bioengineering Conference, 2002* (IEEE, 2002), pp. 171–172.
18. N. V. Ifimtia, B. E. Bouma, J. F. de Boer, B. H. Park, B. Cense, and G. J. Tearney, "Adaptive ranging for optical coherence tomography," *Opt. Express* **12**(17), 4025–4034 (2004).
19. G. Maguluri, M. Mujat, B. H. Park, K. H. Kim, W. Sun, N. V. Ifimtia, R. D. Ferguson, D. X. Hammer, T. C. Chen, and J. F. de Boer, "Three dimensional tracking for volumetric spectral-domain optical coherence tomography," *Opt. Express* **15**(25), 16808–16817 (2007).
20. A. B. Vakhtin, D. J. Kane, W. R. Wood, and K. A. Peterson, "Common-path interferometer for frequency-domain optical coherence tomography," *Appl. Opt.* **42**(34), 6953–6958 (2003).
21. Y. Huang, K. Zhang, J. U. Kang, D. Calogero, R. H. James, and I. K. Ilev, "Noncontact common-path Fourier domain optical coherence tomography method for in vitro intraocular lens power measurement," *J. Biomed. Opt.* **16**(12), 126005 (2011).
22. J. U. Kang, J. H. Han, X. Liu, K. Zhang, C. G. Song, and P. Gehlbach, "Endoscopic functional Fourier domain common path optical coherence tomography for microsurgery," *IEEE J. Sel. Top. Quantum Electron.* **16**(4), 781–792 (2010).
23. K. M. Tan, M. Mazilu, T. H. Chow, W. M. Lee, K. Taguchi, B. K. Ng, W. Sibbett, C. S. Herrington, C. T. A. Brown, and K. Dholakia, "In-fiber common-path optical coherence tomography using a conical-tip fiber," *Opt. Express* **17**(4), 2375–2384 (2009).
24. K. Zhang, W. Wang, J. H. Han, and J. U. Kang, "A surface topology and motion compensation system for microsurgery guidance and intervention based on common-path optical coherence tomography," *IEEE Trans. Biomed. Eng.* **56**(9), 2318–2321 (2009).
25. K. Zhang and J. U. Kang, "Common-path low-coherence interferometry fiber-optic sensor guided microincision," *J. Biomed. Opt.* **16**(9), 095003 (2011).
26. C. Song, P. Gehlbach, and J. U. Kang, "Active Tremor Cancellation by a "Smart" Handheld Vitreoretinal Microsurgical Tool Using Swept Source Optical Coherence Tomography," *Opt. Express* **20**(21), 23414–23421 (2012).
27. Y. Watanabe and T. Itagaki, "Real-time display on Fourier domain optical coherence tomography system using a graphics processing unit," *J. Biomed. Opt.* **14**(6), 060506 (2009).
28. Y. Huang, X. Liu, and J. U. Kang, "Real-time 3D and 4D Fourier domain Doppler optical coherence tomography based on dual graphics processing units," *Biomed. Opt. Express* **3**(9), 2162–2174 (2012).
29. Y. Huang, K. Zhang, C. Lin, and J. U. Kang, "Motion compensated fiber-optic confocal microscope based on a common-path optical coherence tomography distance sensor," *Opt. Eng.* **50**(8), 083201 (2011).
30. R. Leitgeb, W. Drexler, A. Unterhuber, B. Hermann, T. Bajraszewski, T. Le, A. Stingl, and A. Fercher, "Ultrahigh resolution Fourier domain optical coherence tomography," *Opt. Express* **12**(10), 2156–2165 (2004).
31. J. Y. Ha, M. Shishkov, M. Colice, W. Y. Oh, H. Yoo, L. Liu, G. J. Tearney, and B. E. Bouma, "Compensation of motion artifacts in catheter-based optical frequency domain imaging," *Opt. Express* **18**(11), 11418–11427 (2010).
32. J. Lee, V. Srinivasan, H. Radhakrishnan, and D. A. Boas, "Motion correction for phase-resolved dynamic optical coherence tomography imaging of rodent cerebral cortex," *Opt. Express* **19**(22), 21258–21270 (2011).
33. E. A. Swanson, J. A. Izatt, M. R. Hee, D. Huang, C. P. Lin, J. S. Schuman, C. A. Puliafito, and J. G. Fujimoto, "In vivo retinal imaging by optical coherence tomography," *Opt. Lett.* **18**(21), 1864–1866 (1993).
34. M. F. Kraus, B. Potsaid, M. A. Mayer, R. Bock, B. Baumann, J. J. Liu, J. Hornegger, and J. G. Fujimoto, "Motion correction in optical coherence tomography volumes on a per A-scan basis using orthogonal scan patterns," *Biomed. Opt. Express* **3**(6), 1182–1199 (2012).
35. D. D. Duncan and S. J. Kirkpatrick, "Processing algorithms for tracking speckle shifts in optical elastography of biological tissues," *J. Biomed. Opt.* **6**(4), 418–426 (2001).
36. R. A. McLaughlin, B. C. Quirk, A. Curatolo, R. W. Kirk, L. Scolaro, D. Lorenser, P. D. Robbins, B. A. Wood, C. M. Saunders, and D. D. Sampson, "Imaging of breast cancer with optical coherence tomography needle probes: feasibility and initial results," *IEEE J. Sel. Top. Quantum Electron.* **18**(3), 1184–1191 (2012).
37. D. Lorenser, X. Yang, and D. D. Sampson, "Ultrathin fiber probes with extended depth of focus for optical coherence tomography," *Opt. Lett.* **37**(10), 1616–1618 (2012).

## 1. Introduction

Optical coherence tomography (OCT) is a non-invasive, high speed, high-resolution, three-dimensional imaging modality that is widely being used for biomedical applications [1,2]. The real-time non-invasive depth-resolved imaging of tissue structure and flow information provided by OCT can be highly valuable information that can assist physicians in making real-time decisions during surgical procedures such as neurosurgery, tumor resection, microvascular anastomosis, and retinal microsurgery [3–9].

In many circumstances, it is more convenient to use a simple hand-held, manually-scanned probe to obtain OCT images of tissues and organs which might otherwise be inaccessible using standard mechanical scanning heads [6]. A hand-held imaging probe has the following advantages. First, it is small and lightweight, making it easy to access tight spaces. Second, surgeons are intimately familiar with hand-held instruments that can leverage their experience and skills with little training. Third, a small hand-held instrument offers greater safety because the surgeon can more easily override or remove the instrument in cases of malfunction [10]. Finally it offers the surgeon great freedom to obtain any image size, for example a larger field-of-view compared to those constrained by apertures of scanning lens or other endoscopic probes [11–15].

A hand-held probe, however, poses additional challenges over mechanically-rigid scanners. First, non-uniform motion of the probe during lateral manual scanning will cause image distortion and inaccuracy. Earlier work by Ahmed et al. and more recent work by our lab provide solutions to correct non-uniform scanning speed artifact using de-correlation of adjacent A-lines [6,16]. Second, physiological tremor composed of low and high frequency amplitudes over 100  $\mu\text{m}$  would cause large motion artifacts in acquired images [17]. Involuntary motions of a subject may also cause OCT imaging artifacts. Finally, the manual scan across and close to the target surface is highly risky—especially involving fragile tissues. For example, in the context of retinal surgery, the retina is only  $\sim 350\ \mu\text{m}$  for humans, and tearing it can permanently damage eyesight. Scanning while maintaining a larger distance between the probe tip and target surface is not an ideal solution since that degrades image quality and the imaging depth is typically limited to 3-5 millimeters. While motion is in the form of both axial and lateral directions, axial motion is the primary concern due to its direct effects on the image quality. There have been methods used to compensate for the sample surface topology and axial motion in OCT to keep a good system sensitivity and image range, for example adaptive ranging technique for time-domain OCT (TDOCT) [18] and the reference mirror tracking method for spectral domain OCT (SDOCT) [19]. Common path optical coherence tomography (CP-OCT) is a simple, all-fiber-based technique that shares reference and probe arm which circumvents group velocity dispersion and polarization compensation [20]. With all-fiber setup it has been widely studied for various medical applications because it can be arbitrary long, which is of great importance in the clinical environment [21–23]. Recently, CP-OCT has been demonstrated for surface topology and motion compensation [24] and a conceptual micro-incision tool [25], and novel microsurgical tool platform which is called "SMART" (smart micromanipulation aided robotic-surgical tool), active tremor cancellation based handheld vitreoretinal microsurgical tool [26].

In this work, we developed and studied a CPOCT-based hand-held imaging system capable of motion compensation in the axial direction. A prototype hand-held imaging probe that housed a piezoelectric motor and an imaging fiber tip has been fabricated and tested. Distance from the fiber tip to the imaging target was monitored and adjusted by the corresponding feedback control of the motor. In principle the mechanism utilized to compensate axial motion is straightforward and similar to adaptive ranging or the reference mirror tracking method. However, combining this mechanism with a spectral domain CPOCT

system by moving the imaging tip solved the problem of degraded lateral resolution with increasing imaging depth. Ten times zero-padding of the A-scan spectrum was used to increase the distance sensitivity to 0.16  $\mu\text{m}$  in our system, thus yielding better motion compensation performance. Graphical user interface, real-time data processing, and visualization based on a CPU-GPU hybrid programming architecture [27,28] were also developed. Hand-held manual scan images of two artificial phantoms, human hand palm, finger nail and *ex vivo* bovine retina were obtained. We used a cross-correlation maximization based shift correction algorithm for topology correction to provide anatomically correct images to surgeons, since the system flattens the acquired image. The system was able to track the sample surface with a rate of 460 Hz and the root-mean-square (RMS) error of a hold-still task was measured to be 2.93  $\mu\text{m}$ . To the best of our knowledge, this is the first time that a probe capable of compensating axial motion for image formation in hand-held manual-scanning OCT being reported.

## 2. Methods

### 2.1. System configuration

The system configuration and schematic diagram of the prototype probe are shown in Fig. 1 (a). A right angle cleaved single-mode fiber was inserted into an inner needle with a slight recession to protect the fiber end facet. The inner needle (25-gauge, BD Syringe) was attached to a piezoelectric linear motor while the outer needle (20-gauge, BD Syringe) was used to guide the movement of the inner needle [26]. The motor and CP-OCT system formed a closed-loop control system. A design illustration of the prototype probe used in this study is shown in Fig. 1(b) and a photograph of the prototype probe is shown in Fig. 1(c). The length of aluminum probe is 140 mm excluding attached needle; its weight is about 65 g. Such a light weight gives the surgeon negligible burden to move it around. A zoomed view of the probe needle set tip is shown in Fig. 1(d) and Fig. 1(e).

We used a fiber pigtailed 635 nm red diode laser (Meshtel, MFM-635-2S) as a guide. Light from a SUPERLUM Broadband Light Source (center wavelength: 845 nm, bandwidth: 105 nm) was coupled into a single-mode fiber probe by a 50/50 broadband coupler. The distal end of the single-mode fiber (5.6/125  $\mu\text{m}$  Core/Clad diameter) probe was cleaved at a right angle to provide a Fresnel reflection that served as the reference. The single-mode fiber reference surface was protected by leaving the fiber tip inside the tube. The back-reflected/scattered light from the sample was collected by the bare fiber probe and routed to an in-house-built spectrometer. We used a 12-bit, 2048 pixel CCD line-scan camera (e2v, EM4, USA) with a camera link interface as the detector of the home-built spectrometer. The minimum line period limited by the camera is 14.2  $\mu\text{s}$ , corresponding to a maximum line rate of 70,000 A-scans/s. The spectrum data acquired by the camera is transferred to a computer through a frame grabber (National Instruments, PCI-E 1429). In the following experiment, each A-line is an average of three A-scans; this was used for tracking the probe tip movement relative to the target surface. The eventual compensation rate of the system was determined by the frame rate of the system, which was less than the maximum line rate. The CP-OCT system has an axial resolution of 3.6 micron in air and 2.8 micron in water. Using the peak detection, we achieved a calibrated position accuracy of 1.6 micron [29]. To further increase the distance-sensing accuracy of the system, we applied the ten times zero-padding technique [30] to achieve a theoretical accuracy of 0.16 micron, sufficient for us to do the motion compensation. Please note that accuracy and resolution of an imaging system are different. Resolution describes the smallest separation of two targets that can be detected, while accuracy describes the smallest displacement of only one target that can be resolved. The lateral resolution depends on the distance from the sample to the fiber tip. The lateral resolution is 10  $\mu\text{m}$  at 100  $\mu\text{m}$  away from the fiber tip and increases almost linearly to 33  $\mu\text{m}$  at 1.6 mm away from the fiber tip while our system designed axial imaging range is 1.6 mm.

The single-mode fiber probe was then connected to the shaft of a high-speed linear motor (LEGS-L01S-11, Piezo LEGS). We used a quad-core Workstation (DELL, Precision T7500) to obtain the distance information from the CP-OCT signal and deliver commands to the linear motor through a motor driver. The LEGS-L01S-11 has a 35-mm travel range, 20-mm/s maximum speed, better than 1-nm resolution depending on different control modes, and a 10N maximum driving force. For our experiment, we used a motor with a step resolution of 0.2  $\mu\text{m}$ . While A-scans were used to extract distances from the fiber tip to the sample surface, they were also stored to form M-scan images.

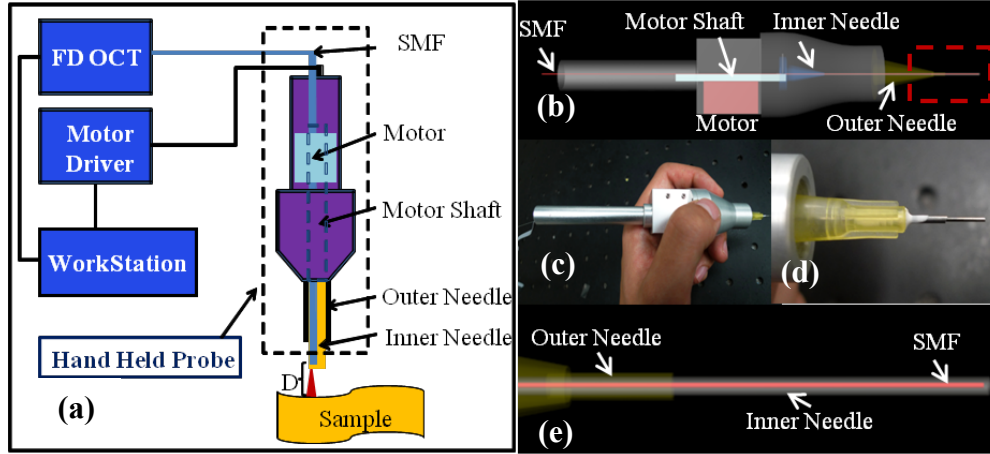


Fig. 1. (a) schematic of system setup; (b) illustration of design of the probe; (c) probe prototype held by hand; (d) zoomed view of the probe needle tip; (e) zoomed view of the dashed red box in (b).

## 2.2. Motion compensation and M-scan imaging

During the hand-held operation, voluntary and involuntary movements of the hand and tissue sample causes the distance,  $D$ , between the fiber tip and the sample surface to deviate from the desired set-point,  $d_0$ , which causes a measured error  $e = D - d_0$ . Based on the measured error,  $e$ , a well-known feedback control approach using PID (Proportional, Integral and Derivative) gain was implemented to control the speed of the piezoelectric motor  $u_m$  to reduce the error:

$$u_m = K_p e + K_I \int e + K_D \frac{d}{dt} e \quad (1)$$

where  $K_p$ ,  $K_I$  and  $K_D$  are respectively the proportional, integral and derivative gain coefficients and were empirically optimized.

We performed M-scan imaging while surface tracking and motion compensation were on. We implemented a real-time, graphical user interface that controls data acquisition, data processing, motion compensation, and image visualization based on a multi-threaded CPU-GPU hybrid programming architecture. The data processing flowchart of the proposed system is shown in Fig. 2. Thread 1 handled the data acquisition from the spectrometer. Thread 2 performed the data processing and motion compensation. Thread 3 performed the image visualization task. Communication and synchronization between the threads are performed through an event-driven method. Computing tasks were distributed among GPU and CPU to take advantage of both processors. Process steps that can achieve better performance through parallel computing were assigned to GPU (outlined by black rectangular), while process steps that require more logical computing were assigned to CPU (outlined by blue rectangular). After the raw spectrum was transferred to the GPU buffer, it was first subtracted by a pre-

acquired physical reference spectrum, and then was cubic interpolated from the  $\lambda$  domain to the  $k$  domain. After that a ten times zero-padding was applied to the interpolated data to increase the distance sensitivity. Three A-scans of post-FFT data of the zero-padded spectrum were averaged to increase the SNR of the A-line data. Due to the ten times zero padding, the post-FFT A-line was shrunk back to normal size and then brightness and contrast adjustment was applied to the shrunk A-line for display purposes. Meanwhile the non-shrunk averaged A-line with higher distance sensitivity was transferred back to the CPU host for the purpose of peak detection and motion compensation. In the following test the CCD camera was running at 460 fps, which corresponds to a motion compensation rate of 460 Hz with 2.2 ms interval. This gives an effective sampling rate of 460 A-scans per second while the hand is moving the probe.

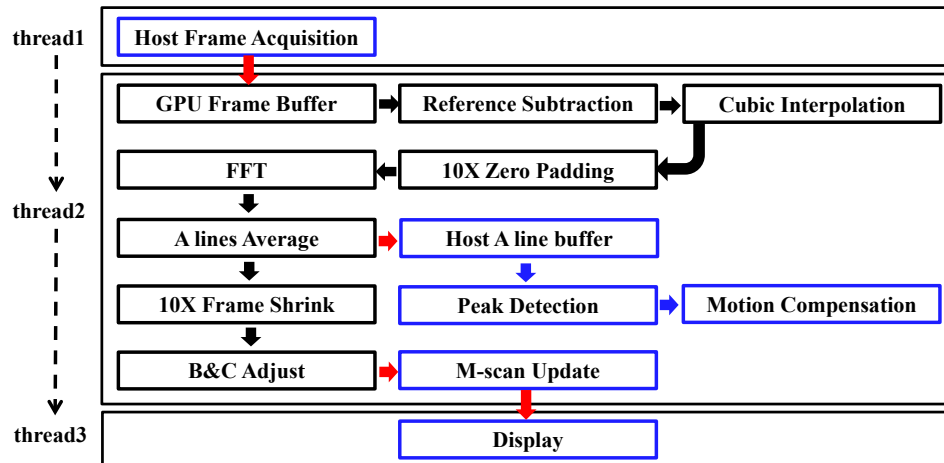


Fig. 2. Data processing flowchart: red arrows indicate data transfer between GPU and host; blue arrows indicate processing flow in host; black arrows indicate processing flow in GPU; GPU kernel functions are outlined with black lines, and CPU functions are outlined with blue lines; dashed arrows indicate triggering between the three threads.

### 2.3. Topology correction

The motion compensation function of the probe tries to keep the distance between the imaging fiber tip and sample surface constant during the OCT imaging, which eliminates the motion artifacts due to hand and sample motions, and the sample surface topology. While suppression of the hand and sample motions is desirable, removal of the surface topology is a side effect that needs to be addressed. The motion compensation algorithm includes Doppler velocity-based correction [31] and image structure intensity based position correction [32–34]. In this work, we performed the topology correction by shifting certain number of pixels ( $\Delta z$ ) in the axial direction to maximize the cross-correlation between adjacent A-scans for its simplicity and effectiveness. This method was evaluated [32] for bulk image shifts (BISs) correction. The pseudo-code of the topology correction process is illustrated in Fig. 3. For an image consisting of  $N$  number of A-scans, an array of size  $N-1$  containing  $\Delta z_n$  will be created. As shown in Eq. (2),  $F(\Delta z)$  is a cross-correlation (XOR) function with variable  $\Delta z$  indicating the pixel-shift amount between A-line( $n$ ) and A-line( $n + 1$ ), while  $n \in [1, N-1]$ . A-line( $n$ ) indicates the number  $n$  A-line out of the total  $N$  A-lines in the frame image. By iterating  $\Delta z$  from  $-\Delta z_{\text{range}}$  to  $+\Delta z_{\text{range}}$  with incremental step size of one,  $\Delta z_n$  will be recorded as the value that maximize  $F(\Delta z)$ .  $\Delta z_{\text{range}}$  determines the time cost to  $\Delta z_n$ . The larger it is, the longer it takes to find  $\Delta z_n$ . Here we chose  $\Delta z_{\text{range}}$  to be 20, which corresponds to a relative displacement of 32  $\mu\text{m}$ , then considering the sampling rate of 460 A-scans per second, this corresponds to an axial motion speed of  $\pm 14.72$  mm/s between adjacent A-scans. This speed range is sufficient for us to correct the relative axial motion speed induced by hand tremor or target

motion. Then, using the first A-line as the origin ( $Z_1 = 0$ ), the total amount of pixel shift  $Z$  for A-line( $m$ ) is the summation from  $\Delta z_1$  to  $\Delta z_{m-1}$ ,  $m \in [2, N]$ , shown in Eq. (3). By shifting A-line( $m$ ) with the corresponding  $Z_m$  in the axial direction for all the A-lines in the frame, the final topology correction image is achieved. The assumption for this method working properly is that adjacent A-scans of biological tissue exhibit maximum cross-correlation under a natural topology state, which is intuitive [35] and that they are correlated, which is satisfied by experimentally oversampling the imaging area.

$$F(\Delta z) = \text{XOR}[A_n(z), A_{n+1}(z + \Delta z)], \quad \Delta z \in [-\Delta z_{\text{range}}, +\Delta z_{\text{range}}], \quad n \in [1, N-1], \quad (2)$$

$$Z_m = \sum_{i=1}^{m-1} \Delta z_i, \quad m \in [2, N]. \quad (3)$$

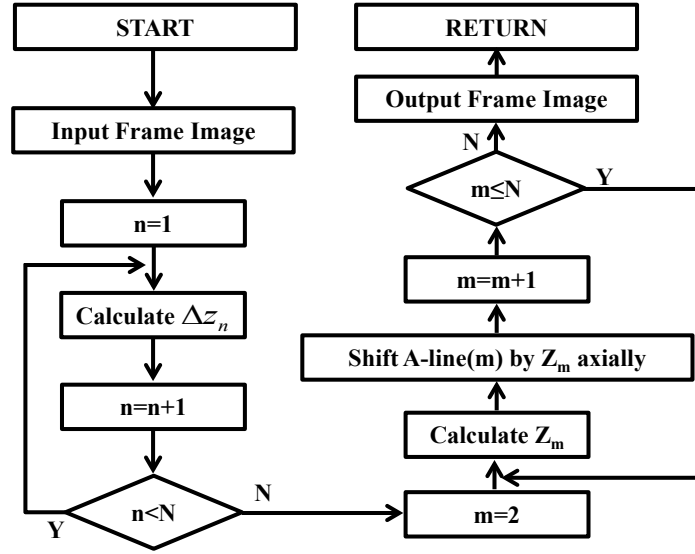


Fig. 3. Pseudo-code of the cross-correlation maximization-based shift correction algorithm.

### 3. Results and Discussion

#### 3.1. Motion compensation test

First, we tested the motion compensation function of our system using a “hold-still” task. The probe was held by one volunteer and pointed perpendicular to a target surface. The operator tried to maintain a constant distance of  $D = 640 \mu\text{m}$  and the probe position was recorded as the function of time. As shown in Fig. 4(a), our feedback control of the motor greatly reduced hand tremor, which is composed of both low frequency drift and high frequency vibration. The system was able to limit the hold-position drift/error to less than the maximum peak-to-peak error of  $\pm 14 \mu\text{m}$  as shown in Fig. 4(b). The RMS error after motion compensation was much lower and was  $\pm 3 \mu\text{m}$ . Figure 4(c) shows the frequency spectrum analysis results of the fiber tip-to-probe distance with (red) and without (blue) motion compensation over a 10-second period. As we can see from the spectrum, the hand tremor has been well suppressed.

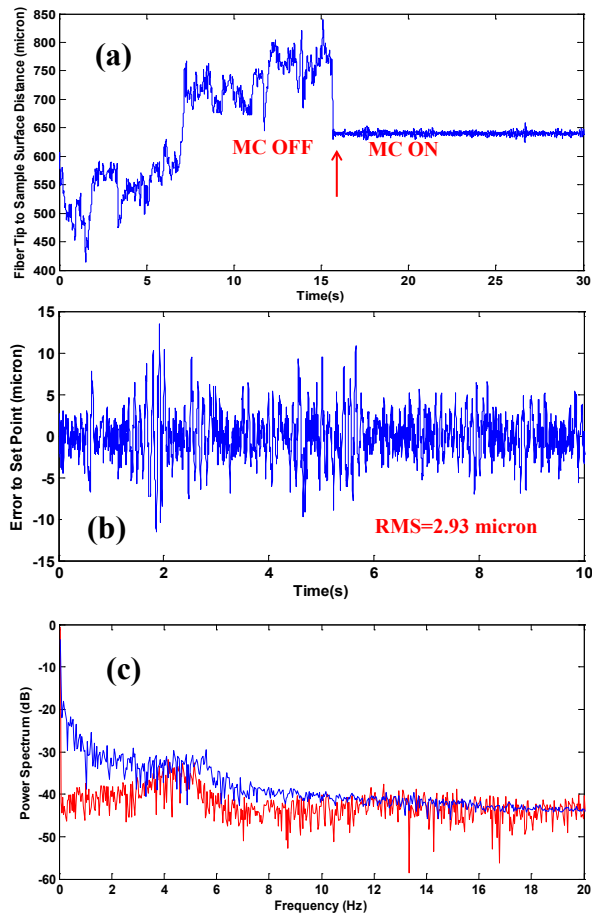


Fig. 4. (a) Free hand-held probe position tracking; (b) zoomed view of motion compensation, time zero corresponding to the red arrow position in (a); (c) frequency analysis 0 to 20 Hz: red (motion compensation is on), blue (motion compensation is off).

### 3.1. Hand-held imaging

To demonstrate that the motion-compensated hand-held probe can significantly enhance the imaging quality of the free-hand scanning OCT system, we performed a series of imaging studies using two phantom samples, *in vivo* tissues, and *ex vivo* bovine retina. The images were cropped for better viewing. Figure 5(a) is a digital camera image of the first artificial sample, which is a resolution card with 1 line per millimeter lines of the card surface. Figure 5(b) is the standard galvanometer-mirror scanned SD-OCT image along the red line mark in Fig. 5(a), the lateral image field of view is 22 mm. From Fig. 5(b) we can clearly see the structure of our sample. On top of the target card we placed two polymer tape layers and then we added five polymer strips separated from each other to form a step-like surface topology. Parallel to the red line mark in Fig. 5(a), is a stainless steel rod used to guide the probe scanning, though it is very difficult to scan the exact same position during this study. Figure 5(c) is the handheld imaging without motion compensation. We can clearly see the hand tremor and thus two important consequences: sample collision and signal loss. Places where the probe collided with the sample were marked in red circles in the image. Figure 5(d) is the topology corrected image of the Fig. 5(c). Figure 5(e) is the handheld imaging with motion compensation. As expected, there was no accidental collision with the sample and the probe tracked the area of interest precisely. Figure 5(f) is the topology corrected image of Fig. 5(e).



From Fig. 5(d) and Fig. 5(f), we can see that cross-correlation based shift correction algorithm can reconstruct the sample surface topology reasonably well. Therefore reconstructed images are much easier to interpret than those images with motion corruption artifacts. That is, the layer structure, detailed structure lied between layers, and the step shape surface structure are all clearly visible. Also, non-uniform lateral scanning speed can be visualized through the non-periodic structure of the underlying lines.

We further evaluated our system performance by imaging another phantom sample having a ridge shaped surface topology, created by placing layered tape on top of a clay. An image using a bulk scanning head is shown in Fig. 6(a). Figure 6(b) shows a handheld imaging without the motion compensation. Since the height of the ridge is large, whenever the probe

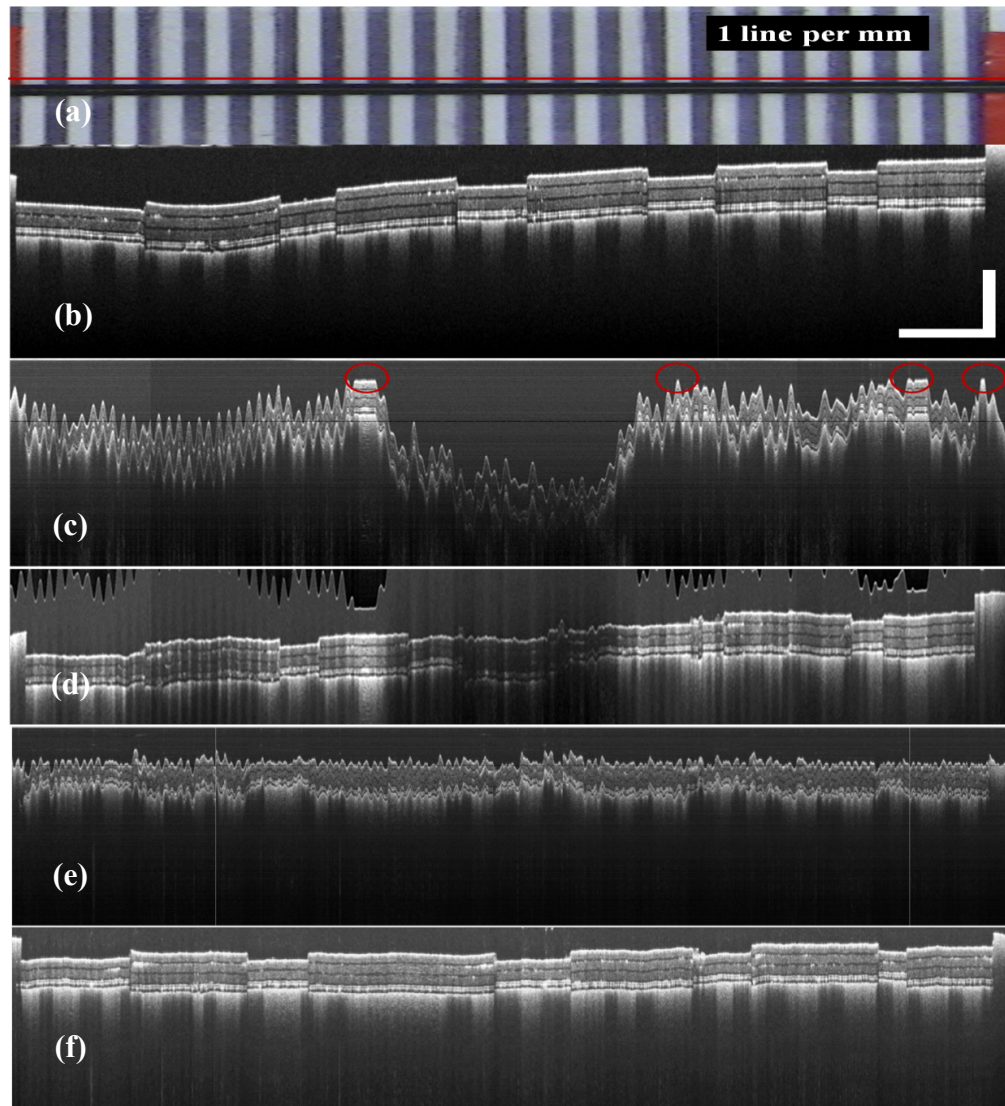


Fig. 5. (a) camera picture of a phantom sample; (b) standard galvanometer-mirror scanned SD-OCT image of the phantom sample along the red line shown in (a); (c) freehand scanned image along the red line without motion compensation, red circles mark where the tool tip collided with the sample surface; (d) topology corrected image of (b); (e) freehand scanned image along the red line with motion compensation; (f) topology corrected image of (e). (scale bar: vertical 500  $\mu$ m, lateral 2 mm)

tip moved close to the ridge, it collided with the sample. The collision area is marked with a red rectangular box. When the probe collided with the surface the signal faded and the reconstructed image became incorrect over that range. Figure 6(d) is the handheld scanning image with the motion compensation. We were able to scan across the ridge without touching the ridges. Figure 6(e) is the topology corrected image of Fig. 6(d). It is clear that the general ridge shape has been recovered with some error. Notably the flat bottom has been reconstructed into a curved shape. Nevertheless the shape of surface and the underlying structure of the sample can be easily seen. Undoubtedly the software correction method we implemented here doesn't result in a perfect surface topology reconstruction. However, this technology provides an ability to perform free-hand OCT scanning with a needle probe,

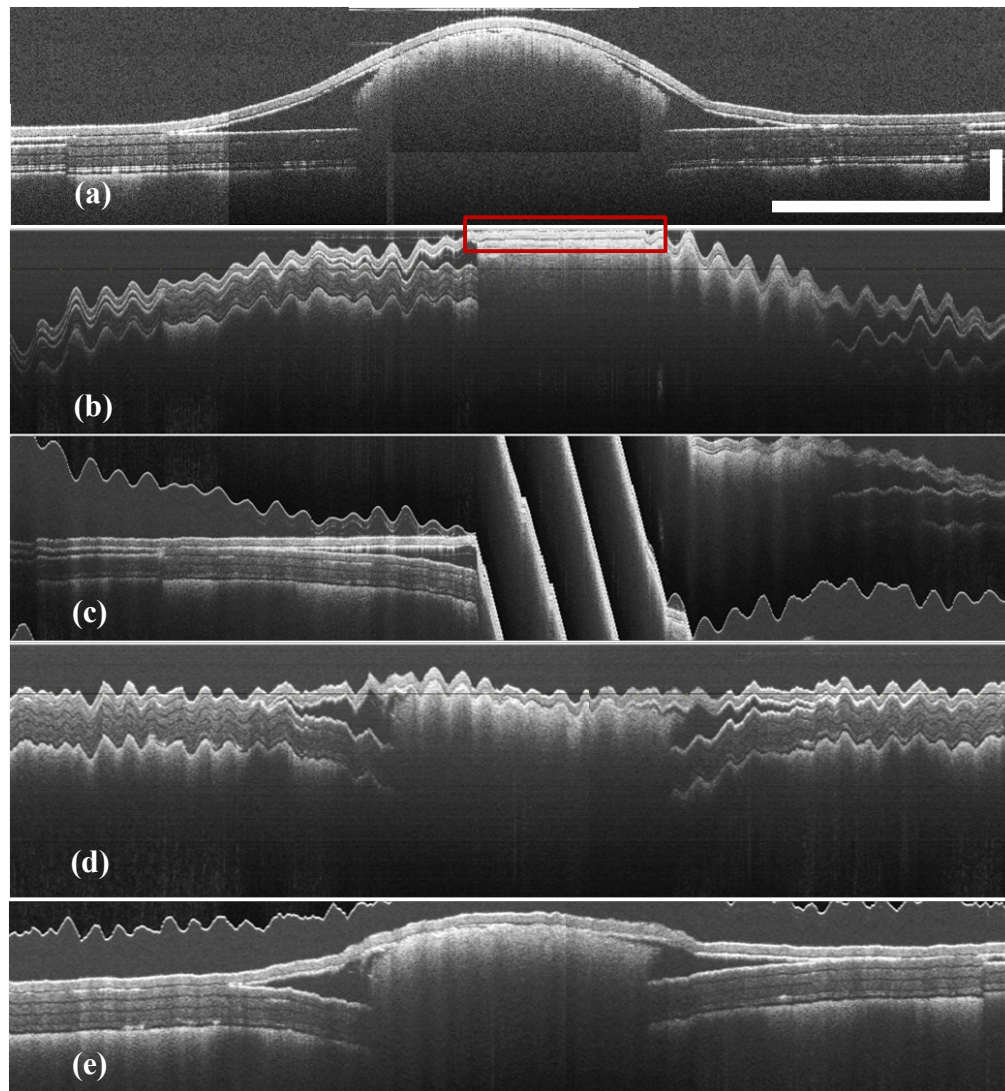


Fig. 6. (a) galvanometer-mirror scanned SD-OCT image of a phantom with ridged surface topology (b) freehand imaging of the sample without motion compensation, red rectangular indicates where the probe collided with the sample surface; (c) topology corrected image of (b); (d) freehand imaging of the sample with motion compensation; (e) topology corrected image of (d). (scale bar: vertical 500  $\mu\text{m}$ , lateral 2 mm)

provides a large field of view, and significantly reduces the chance of accidental tool tip collision with tissue.

We further tested our system by imaging a non-stationary, naturally placed palm of the hand and finger nail; the results are shown in Fig. 7 and Fig. 8. Estimated lateral scanning range is 15 mm for Fig. 7 and 8 mm for Fig. 8. The hand tremor is apparent on images without motion compensation, Fig. 7(a) and Fig. 8(a). Accompanied with hand tremor was the non-uniform intensity variation over the scanned images. When the probe distance increases, A-lines become dimmer and sometimes get completely lost. One extreme case is shown in the

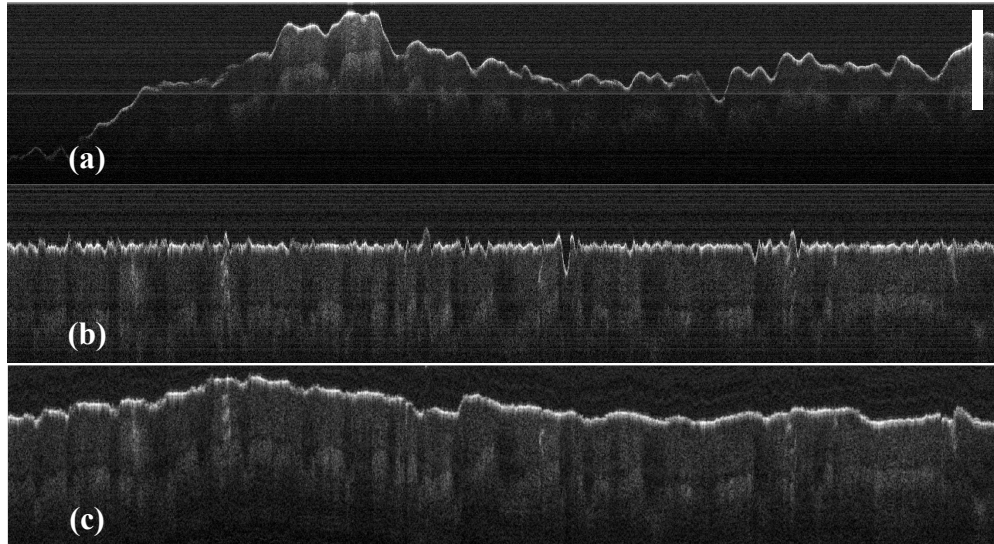


Fig. 7. Hand-held imaging of human hand palm without (a) and with (b) motion compensation; (c) topology-corrected image for (b) (scale bar: 500  $\mu\text{m}$ )

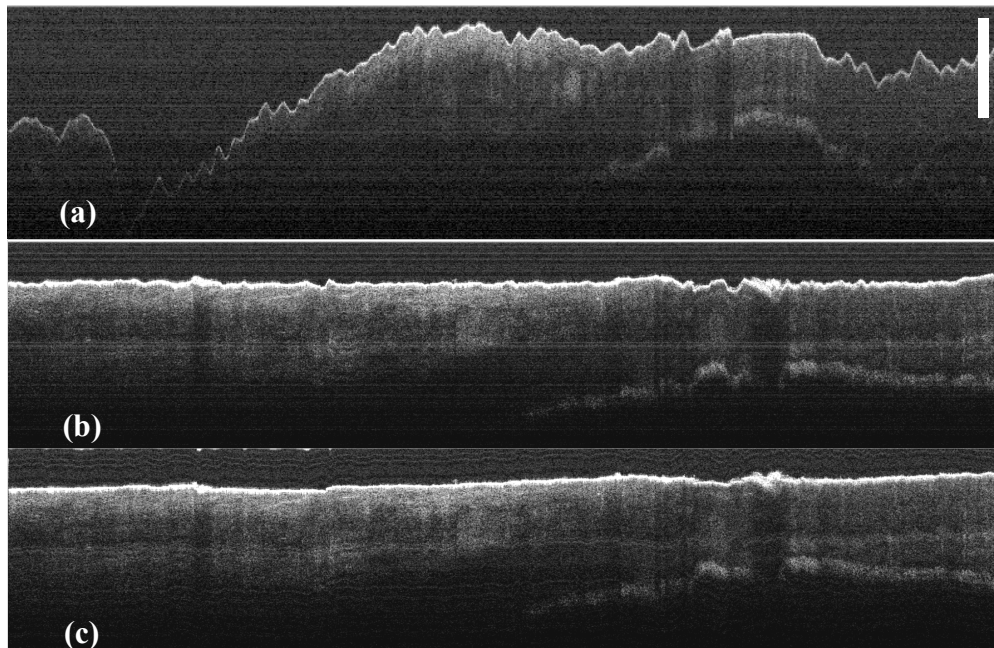


Fig. 8 Hand-held scanning of human finger nail without (a) and with (b) motion compensation; (c) topology-corrected image for (b) (scale bar: 500  $\mu\text{m}$ )



left part of Fig. 7(a) and Fig. 8(a): the probe is so far away from the tip that detailed structure or anatomy information beneath the target surface was not imaged. The effect of motion compensation can clearly be seen from images in Fig. 7(b) and Fig. 8(b). The low frequency axial drift was almost completely negated while the amplitude of high frequency vibration was well compressed. Detailed structures of the hand palm and finger nail are clearly visible. We can clearly see the boundary between epidermises and dermises layers and sweat duct lying within the epidermises layer. Due to the wavy surface topology of hand palm, the probe compensates more when the hand palm was imaged compared to the finger nail. After surface topology correction, Fig. 7(c) revealed the smooth wavy surface topology of hand palm clearly, and the sweat duct in Fig. 7(c) becomes naturally spiral. Figure 8(c) also revealed smooth and natural topology of the finger nails junction area. These performances of our system were consistent with our phantom imaging. Safety is one of the main concerns for the image-guided intervention. By keeping our probe at a constant distance of 200  $\mu\text{m}$ , risk of damaging the sample surface by accidental hand movement was avoided—an important factor which needs to be addressed during image-guided microsurgery intervention.

To further study the probe imaging capability, we performed *ex vivo* bovine retina imaging with vitreous removed as shown in Fig. 9. Estimated lateral imaging range was 6 mm. Cow eyes were obtained from a local butcher shop. Figure 9(a) is the image without motion compensation. The probe collision with the retina can be seen from the distorted image areas. Figure 9(b) is the image with motion compensation while Fig. 9(c) is the topology corrected image of Fig. 9(b). This again demonstrates the active distance control's ability to prevent

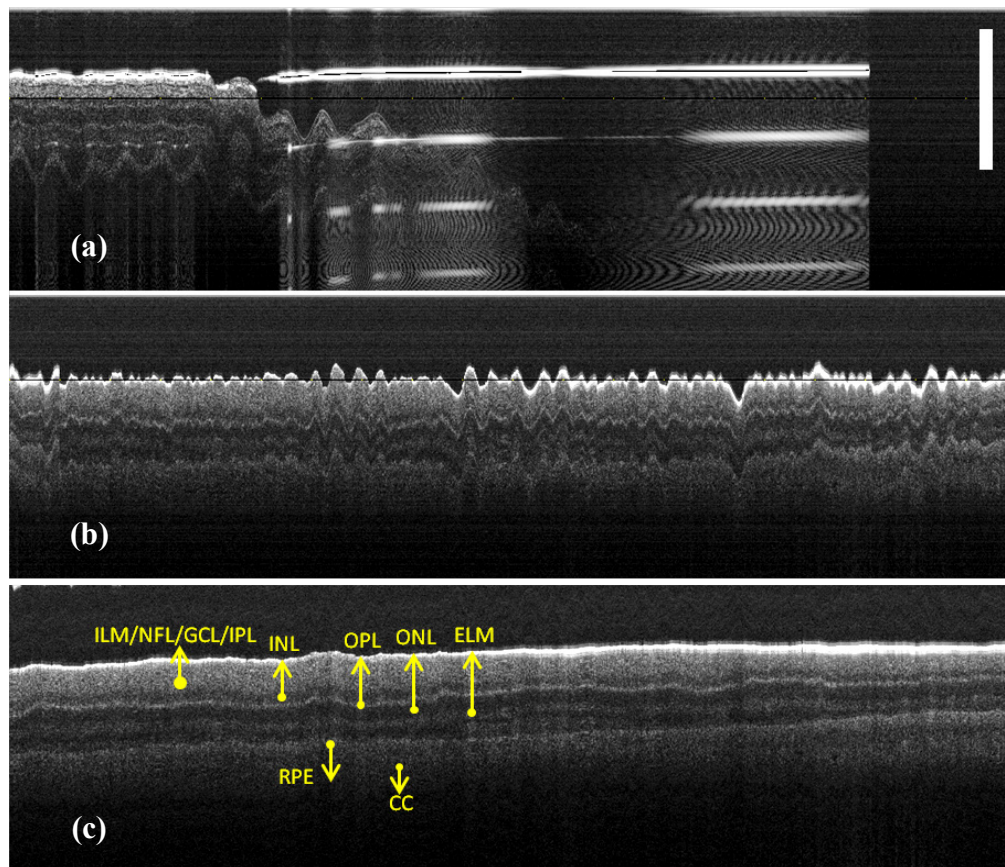


Fig. 9. Hand-held scanning of bovine retina without (a) and with (b) motion compensation; (c) topology-corrected image for (b) (scale bar: 500  $\mu\text{m}$ )

collision between the sample and the probe. Since the eye was imaged several hours after harvesting, the retina degenerated and some retinal layers are less prominent. First four layers of the retina have lost boundaries. All retina layers have been labeled in Fig. 9(c).

Performance of motion compensation is a crucial factor that affects the quality of free-hand scanning OCT systems. In our experiment, we used a piezoelectric motor controlled OCT probe to provide the motion compensation through a USB com port interface with baud rate of 9600 bits/s. Command delivery through USB cable consists of 19 bits: 8 of them are used to control the time cost of one motor step; 10 of them are used to control how many steps to move during one command, while 1 bit of them is the stop bit, which gave us the maximum compensation rate of around 505 Hz. During our experiment, the compensation rate varied from 450 Hz to 470 Hz. We confirmed the compensation rate by continuously sending commands to the motor and recording the time cost in C++ without any other computation task involved. The result was 500 Hz, which corresponds well with the 505-Hz limit. The command delivery latency through the USB port was one of the bottlenecks. Another important factor that affected the motion compensation result was our system distance sensitivity. It is easy to compensate for small errors, but this would require better distance sensitivity that would enable the system to detect these smaller errors. We applied a  $10\times$  zero-padding to the spectrum, which effectively improved the system distance sensitivity by a factor of 10: from 1.6  $\mu\text{m}$  to 0.16  $\mu\text{m}$ . However, such digital processing method cannot improve the system sensitivity indefinitely [26]. As the time-varying M-scan images were recorded, there was a non-uniform spatial sampling rate in lateral direction due to the non-constant scanning velocity of hand-held scanning. Though this is not the focus problem of this manuscript—and the resulting images we got did not suffer a lot from this non-constant scanning speed—this needs to be addressed in the future. The motion-compensation process results in flat images, which eliminates the topographical information of the target surface; therefore we implemented a simple and intuitive cross-correlation maximization-based shift correction algorithm to restore the target topology. Further study on the topology correction algorithm such as Doppler velocity-based algorithms and registration algorithms based on different global objective functions [34] will be performed later. As both the lateral non-uniform scanning speed correction and topology correction utilize the cross-correlation information between adjacent A-scans, studies combining both axial and lateral scanning correction will be carried out in the future.

It needs to be pointed out that the bare fiber probe has several limitations, such as fixed reference level, decreased lateral resolution with the increase of imaging depth, and relatively low signal collection efficiency. Therefore our system was designed to operate within an imaging depth of 1.6 mm. If the system requires a longer imaging depth, for example, 3–4 mm, an optical system [36,37] needs to be implemented at the distal end of the probe. We have recently demonstrated that sapphire ball-lensed probes show significant improvements in terms of imaging quality and working distance [38].

#### 4. Conclusion

We have developed a hand-held, manual-scanning OCT system capable of compensating hand tremor and tracking target surface for the first time to the best of our knowledge. The system operates at a compensation rate of 460 Hz with RMS error of 2.93  $\mu\text{m}$ . Images from artificial samples and *in vivo* hand palm and finger nail, and *ex vivo* bovine retina were obtained, which showed greatly reduced hand tremor artifacts. We corrected the sample surface topology through a cross-correlation maximization-based shift method. Moreover, the system could significantly reduce the risk of tearing the target surface. Future work would involve further optimizing the motion compensation and topology correction algorithm, combining the topology correction together with non-uniform lateral scanning speed correction and probe optics optimization. Eventually we plan to test the system performance during microsurgical interventions.

### **Acknowledgments**

This work is funded by NIH/NEI 1R01EY021540-01A1. Yong Huang is partially supported by the China Scholarship Council (CSC). We would like to thank Mingtao Zhao and Saumya Gurbani for fruitful discussion.